Nano Energy 51 (2018) 206–215

Contents lists available at ScienceDirect

Nano Energy

journal homepage: www.elsevier.com/locate/nanoen

Full paper

A comprehensively theoretical and experimental study of carrier generation and transport for achieving high performance ternary blend organic solar cells

Zi Shuai Wang[a], Xingang Ren[a], Xiaopeng Xu[b], Qiang Peng[b], Wei E.I. Sha[a], Wallace C.H. Choy[a,*]

[a] Department of Electrical and Electronic Engineering, The University of Hong Kong, Pokfulam Road, Hong Kong, China
[b] Key Laboratory of Green Chemistry and Technology of Ministry of Education, College of Chemistry, and State Key Laboratory of Polymer Materials Engineering, Sichuan University, Chengdu 610064, PR China

ARTICLE INFO

Keywords:
Ternary organic solar cells
Drift-diffusion model
Exciton delocalization
Charge transfer
Exciton transfer

ABSTRACT

Ternary blend organic solar cells (OSCs) composed of three components in the active layer shows the potential to achieve higher power conversion efficiency (PCE) as compared to the binary counterpart due to the wider absorption spectrum, higher generation rate, and better morphology. However, the physical understanding of carrier generation and transport processes in the ternary blend OSCs has been limited explored. In the work, together with experimental studies of the two donors, one acceptor ternary blend OSCs with PCE > 12%, we will theoretically and experimentally describe the roles of the carrier generation (including exciton transfer, delocalization and dissociation), and carrier transport (particularly the hole transport) on the performance of ternary blend OSCs. Through theoretical and experimental investigations, critical design rules for improving the device performance are concluded: (1) improving the exciton delocalization ratio via donor ratio optimization with physical understanding, (2) selecting the donors with well overlap of emission and absorption spectra to promote a beneficial exciton transfer, (3) engineering the energy level of donors to form the blocking barrier for reducing hole transfer into the donor with high recombination loss. The work unveils the device physics which is fundamentally important for designing and optimizing high-performance ternary blend OSCs.

1. Introduction

According to detailed balance theory [1,2], the dominant efficiency loss of a solar cell lies at the spectrum loss. Only photons with energy larger than the band gap of active semiconductor materials will be sufficiently absorbed and converted to electron-hole pair. Thus, fully exploiting sun spectrum in a broadband range is essential to elevate the power conversion efficiency (PCE) of a solar cell system. Recently, ternary blend active layer structure has been intensively investigated in bulk-heterojunction (BHJ) organic solar cells (OSCs) for utilizing the wide spectrally distributed solar irradiation [3–11]. Different from the optimization designs for traditional binary donor: acceptor system, ternary blend OSCs contain the third component in the active layer, and the third component with the complementary absorption spectrum to the binary one, which can be a polymer or small molecule [3,9], offer better matching to the solar spectrum and improve the total absorption. Furthermore, by careful material selection and device fabrication, the incorporation of the third component can improve the morphology of the active layer, so that higher carrier mobility and more efficient carrier generation can be achieved [10]. By taking such advantages, ternary blend OSCs have reached the state-of-the-art PCE of about 14% [12,13], highlighting their great potentials in the field.

The working mechanism of ternary blend OSCs has attracted a lot of interest from both the theoretical and experimental researchers. Several alternative working principles of the ternary OSCs have been proposed, based on different assumptions including the alloy model, parallel-linkage model or sensitizer model [10,14–16]. All of these models qualitatively explain some of the properties of ternary blend OSCs. However, there are still issues that cannot be clearly and quantitatively described, such as the exciton generation, dissociation, and transfer, as well as the carrier transport and transfer, which are critically important in understanding and optimizing the ternary blend OSCs.

The ternary blend OSCs can be simply divided into two categories: two donors/one acceptor ($D_1/D_2/A$) and two acceptors/one donor ($A_1/A_2/D$) [10]. In $D_1/D_2/A$ system, solar energy can be absorbed by the three components simultaneously, and excitons will be generated in the active layer. Then, the generated excitons will dissociate into the free carriers at the interfaces of D_1/A or D_2/A subsystems. During the

* Corresponding author.
E-mail addresses: qiangpengjohnny@yahoo.com (Q. Peng), chchoy@eee.hku.hk (W.C.H. Choy).

https://doi.org/10.1016/j.nanoen.2018.06.069
Received 10 May 2018; Received in revised form 12 June 2018; Accepted 20 June 2018
Available online 21 June 2018

process, two important excitonic physics concepts of exciton delocalization and exciton transfer are involved, which govern the unique carrier generation mechanism in the ternary blend OSCs.

The first exciton physics is exciton delocalization [17–19]. The exciton behaviors after the photon absorption should be divided into two parts: 1) the ultrafast exciton generation will occur in a very short time regime (< 100 fs) at the interfaces between the donor and acceptor [19,20], and the excited exciton has a very large spatial delocalization, and thus behaves like Wannier exciton, with a large initial exciton radius. The large initial exciton radius indicates the weak Coulomb interaction between the electron and hole, and thus the high dissociation probability. However, the experimental results [18–20] showed that a part of the delocalized excitonic states will collapse to the localized excitonic states at the same time, which behaves like Frankel exciton. 2) The localized excitons will continue to diffuse towards the donor/acceptor interface, forming the charge-transfer (CT) state, and finally dissociate into free carriers. The ratio of the delocalized excitonic states to the total excitonic states plays a very important role in achieving the high performance OSCs [17], while it is intrinsically determined by donor-acceptor material and morphology [20,21]. However, the study of delocalization mechanism in ternary blend OSCs is very limited, and the role of delocalization mechanism in the efficiency improvement of ternary blend OSCs is still unclear.

The exciton transfer physics for the diffusion of localized excitons to the interfaces is considered as the second important excitonic physics. Between the p-type components in ternary blend (i.e. D_1, D_2 in $D_1/D_2/A$ system), the Förster energy-transfer can occur through non-radiative process that are confirmed from the photoluminescence (PL) and absorption spectra [22]. The exciton transfer may change the total exciton dissociation probability afterward determined by the probabilities at D_1/A and D_2/A interfaces. In addition, after the exciton dissociation, the carrier (i.e. hole) transfer may also exist between D_1 and D_2, and can further influence the performance of the ternary blend OSCs. It is because two conducting channels of D_1/A and D_2/A subsystems have different carrier transport properties including mobility, recombination and injection/extraction barriers. Therefore, the carrier transfer between the D_1/A and D_2/A subsystems will influence the total recombination loss and thus the device performance. However, the effects of both exciton and carrier transfer in the ternary blend OSCs have not yet been explored.

In this work, through both experimental and theoretical studies, the carrier generation mechanism includes the exciton delocalization, dissociation and transfer, as well as the charge transfer during the carrier transport process in ternary OSCs, which are very limited studied, will be discussed. The efficiency changes in the physical processes of carrier generation, exciton transfer and hole transfer will be quantified. Our result indicates that the main loss of ternary blend OSCs is the inefficient localized exciton dissociation. In addition, the carrier loss introduced by the detrimental exciton transfer (i.e. exciton transfer from the donor with more efficient exciton dissociation D/A interfaces to the one with less efficient exciton dissociation D/A interfaces) will reduce short-circuit current density (J_{SC}), while the extra recombination loss caused by the disadvantageous hole transfer into the donor with low mobility and high carrier recombination will reduce the open-circuit voltage (V_{OC}) and fill factor (FF). Based on the experimental and modeling results, we outline the systematic design rules i.e. increase the exciton delocalization by optimizing the donor component ratio, select the donor materials with proper overlap of the emission and absorption spectrum to allow beneficial exciton transfer, and engineer the energy level of donor materials to form blocking barrier for inhibiting disadvantageous hole transfer. This work enables to gain the insight of device physics for developing high-performance ternary blend OSCs, which will contribute to promote green energy application.

2. Experimental section

2.1. Device fabrication

The non-fullerene acceptor has the advantages including the tunability of light absorption and energy level, diversity of donor-to-acceptor combination, and large-scale production of acceptor materials, which is the hot topic of ternary blend OSCs. To gain the insights of device physics, here we have fabricated a new type of non-fullerene ternary blend OSCs, which comprises a wide-bandgap non-fullerene acceptor [23] (SFBRCN), a medium bandgap polymer donor (PBDB-T: poly[(2,6-(4,8-bis(5-(2-ethylhexyl)thiophen-2-yl)benzo[1,2-b:4,5-b'] dithiophene))-*alt*-(5,5-(1′,3′-di-2-thienyl-5′,7′bis(2-ethylhexyl)benzo [1′,2′-c:4′,5′-c′]dithiophene-4,8-dione))]), and a low bandgap polymer donor (PTB7-Th). Details of device fabrication are described in this section.

2.1.1. Materials

PTB7-Th was purchased from 1-Material, PDBD-T and SFBRCN were synthesized according to previously reported procedures. [23,24] All other chemicals were purchased as reagent grade and used without further purification.

2.1.2. Devices

The device structure is ITO/ZnO/PBDB-T_{1-x}:PTB7-Th_x:SFBRCN/MoO_3/Ag. Pre-patterned ITO substrates (sheet resistance = 15 Ω sq^{-1}) were sequentially ultrasonicated in detergent, deionized water, acetone, and isopropanol, and then UV-cleaned in a UV-Ozone chamber for 20 min. The ZnO solution (2 M in toluene, diluted by tetrahydrofuran) was spin-coated onto the surface of the ITO substrates at a rate of 5000 rpm for 30 s in the 20 L min-1 dry airflow, and then baked on a hot plate at 100 °C for 10 min to form a thin layer of about 30 nm. Ternary blend films with the fixed D: A ratio of 1:0.8 and the total concentration of 18 mg mL^{-1} in chlorobenzene (adding 0.75 v/v% of 1,8-Diiodooctane, DIO) were prepared by spin-coating at 2000 rpm for 60 s. The thickness of the tannery blend films is about 110 nm. A molybdenum trioxide interlayer (MoO_3, 10 nm) and a silver anode (Ag 100 nm) were finally deposited onto the surface of the active layer in an evaporation chamber under high vacuum ($\leq 10^{-6}$ mbar). The fabrication details of hole-only and electron-only devices can be found in the Supporting Information.

2.1.3. Device measurement

The thickness of the each layer was screened by using a Dektak 6 M surface profilometer. The device area was fixed at 4.0 mm^2. The *J-V* characterization of the devices was carried out on a computer-controlled Keithley 2400 source meter with an Air Mass 1.5 Global (AM 1.5G) solar simulator (XES-70S1, SAN EI Co., Ltd.) as the light source with an irradiation intensity of 100 mW cm^{-2}, which was calibrated by using a standard silicon solar cell. The EQE values were tested with a Newport Model 77890 (Newport Co. Ltd.) during the illumination with a monochromatic light from a xenon lamp. The refractive indices (n, k) of perovskite were performed under a dark ambient environment by using spectroscopic ellipsometry (Woollam). All fabrication and characterization processes, except for the refractive indices and EQE measurements, were conducted in a glove box filled with argon atmosphere (< 0.1 ppm O_2 and H_2O).

2.2. Device modeling

Since a systematic device model to describe carrier generation and transport processes in the ternary blend OSCs has not been explored in details, we will develop a new model together with the series of experiment for studying the carrier and exciton dynamics of ternary blend OSCs. Different to the existing works like the alloy or cascade model [10,14–16], a more realistic assumption is applied to this parallel-like

model, coupled with our experiments: the three components in the ternary blend can perform independently and contact with another components individually, which not only enables the analysis of the different carrier generation and transport in two subsystems, but also did not exclude the discussion of carrier and energy transfer between the donors. The external quantum efficiency (EQE) results of the ternary blend OSCs under different component ratios, as shown in Fig. S1, are similar to the weighted sums of the EQEs of the two D/A subsystems. This indicates that the two D/A subsystems have the almost independent responses, so the parallel-like assumption is valid for our study. The new model is based on the augmented drift-diffusion model, including 1) the augmented continuity equations for electrons in acceptor A and holes in both donor D_1 and D_2, 2) the Poisson's equation for potential distribution, and 3) the diffusion-dissociation equations for localized exciton. We modified the hole transport through the coupled continuity equations and then proposed the hole transfer in D_1 and D_2 by introducing the hole transfer rate terms (See Eqs. (A2)–(A4) in Appendix A). According to the Onsager-Braun theory [25,26], the dissociation probabilities of the localized excitons at the D_1/A and D_2/A interfaces are different, therefore we will model the exciton diffusion and dissociation by introducing another two equations. The localized exciton transfer between the donors is taken into account by introducing the localized exciton transfer rate (See Eqs. (A8) and (A9) in Appendix A). Since the free carrier generation by delocalized exciton occurs in the ultrafast timescale, which is much shorter than the carrier transport and exciton diffusion, the delocalization ratio (ratio of delocalized exciton to the total exciton) is introduced in the model to describe the free carrier generation by the delocalized exciton as a direct generation.

The overall physical processes during the ternary blend OSCs operation can be described by this model, and thus we can obtain the theoretical photovoltaic performance. After photon absorption, the delocalized exciton will be generated, while part of which then directly separate into free carriers. The other part of delocalized exciton will collapse into localized exciton. Once the localized excitons are formed, they will diffuse to D_1/A or D_2/A interfaces and form the CT state to separate. During the diffusion, the exciton transfer between D_1 and D_2 will also happen [10]. After the dissociation of localized excitons at the interfaces, the electrons will transport in the accepter domain and the holes will transport in the two donor domains respectively. Meanwhile, the hole transfer between the two donors D_1 and D_2 occurs [27]. After the transport in the active layer, the carriers (holes and electrons) will travel through the corresponding charge transport layers (MoO_3 and ZnO), and finally arrive their respective electrodes. The details of the governing equations and modeling parameters can be referred in Appendix A. It should be noted that, the energetic disorder and the specific morphological problems like interpenetration are not included in our model, which should be important in the binary blend OSCs [28–31]. That is because the morphological problem in our study can be sufficiently discussed by the parallel-like model, and to our knowledge, there is still no clear evidence that the energetic disorder will have special effects on ternary blend OSCs, compared to the cases of binary blend ones.

3. Result and discussion

The two polymer donors have the complementary absorption spectrum, as shown in Fig. 1, resulting in a broad absorption range in visible light wavelength. The inverted device structure of ITO/ZnO (20 nm) /PTB7-Th_x:PBDB-$T_{(1-x)}$:SFBRCN (100 nm) /MoO_3 (10 nm)/Ag (100 nm) has been fabricated, in which the PTB7-Th/PBDB-T/SFBRCN system will be abbreviated as D_1/D_2/A hereafter. With the increase of PTB7-Th (D_1) amount from 0 to 1, the experimental photovoltaic performance of the ternary blend OSCs are shown in Fig. 2, including the current density-voltage (*J-V*) curve and the detailed photovoltaic parameters. The experimental results show that the best OSC

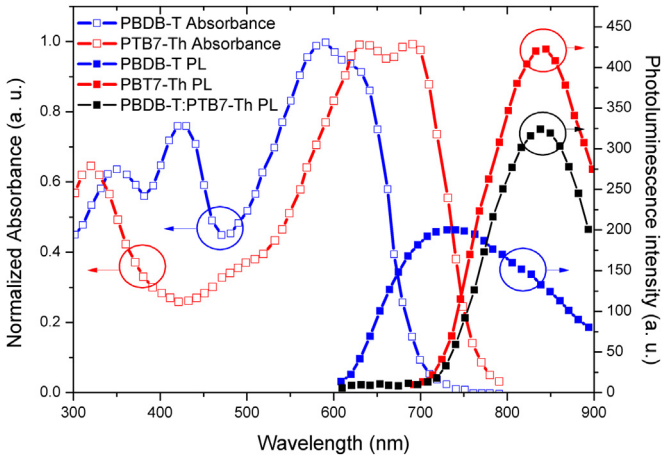

Fig. 1. Experimental PL spectra and normalized absorbance of the PTB7-Th (D_1) and PBDB-T (D_2) polymer and the PL spectra of the PTB7-Th/PBDB-T blend (1:1).

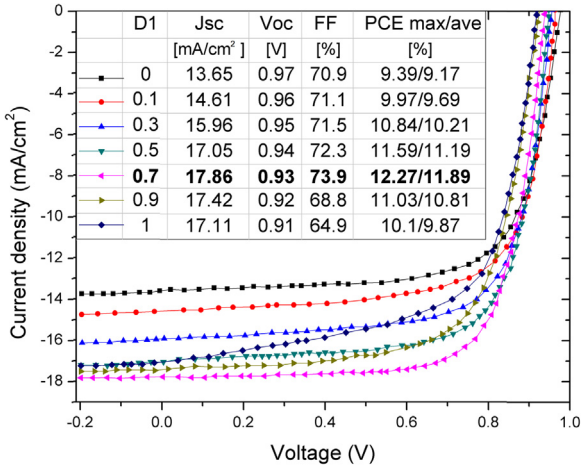

D1	Jsc [mA/cm²]	Voc [V]	FF [%]	PCE max/ave [%]
0	13.65	0.97	70.9	9.39/9.17
0.1	14.61	0.96	71.1	9.97/9.69
0.3	15.96	0.95	71.5	10.84/10.21
0.5	17.05	0.94	72.3	11.59/11.19
0.7	**17.86**	**0.93**	**73.9**	**12.27/11.89**
0.9	17.42	0.92	68.8	11.03/10.81
1	17.11	0.91	64.9	10.1/9.87

Fig. 2. Experimental *J-V* characteristics of ternary blend OSCs with different blend ratios of PTB7-Th under AM 1.5 G 100 mW cm^{-2} illumination. The inset table is the detailed photovoltaic parameters. The averaged PCE values are from at least 20 devices.

performance of the ternary devices is obtained with the 70% blend ratio of PTB7-Th (D_1). V_{OC} monotonously decreases as increasing D_1 amount. Differently, J_{SC} first increases from 13.65 mA cm^{-2} to 17.86 mA cm^{-2} (at 70% blend ratio of D_1), then decreases to 17.11 mA cm^{-2}, fill factor reveals a similar trend as J_{SC} and reaches the peak value of 73.9%. The resultant best PCE of 12.27% is achieved with the ratio of 70% PTB7-Th.

Coupled with the theoretical discussion of device physics of the ternary blend OSCs, the systematic design rules will be put forward in the following sections. The mechanism of free carrier generation, especially the exciton delocalization, are shown in Section 3.1, which indicates the importance of improving the exciton delocalization ratio in the ternary device via the donor ratio optimization. The mechanism of localized exciton transfer, which are mainly related to J_{SC}, as well as the design rule of selecting the materials with proper overlapping of photoluminescence and absorption spectra, are discussed in Section 3.2. The effect of hole transfer between the donors will be analyzed in Section 3.3, which would mainly influence V_{OC} and fill factor. The design rule to improve the V_{OC} and fill factor is also shown in this section. It should be noted that in order to favor the theoretical discussion of the exciton and hole transfers, the ratio of the D_1 and D_2 component in the device simulation is set as D_1:D_2 = 1:1 in Sections 3.2 and 3.3. In Section 3.4, we will discuss and analyze the overall

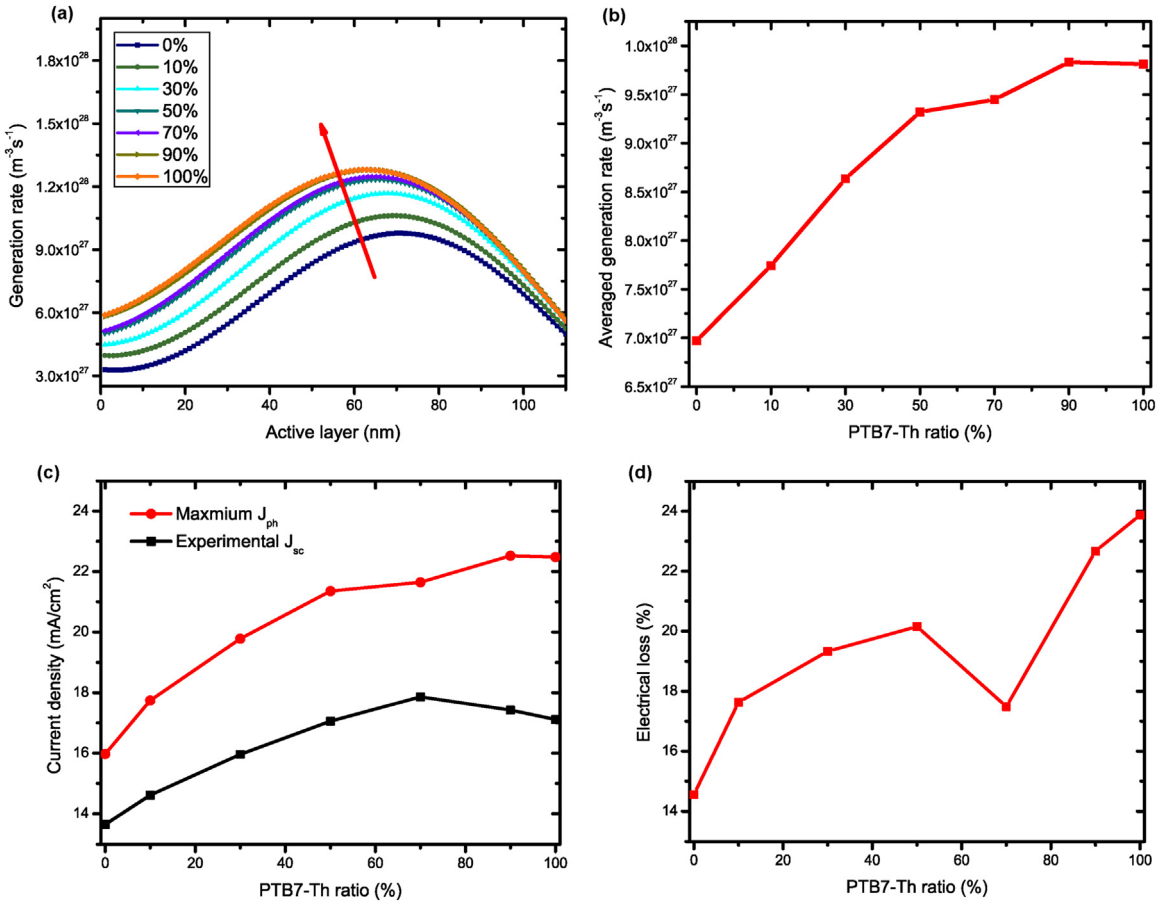

Fig. 3. Generation rate distribution of the ternary blend system in different locations of the file and PTB7-Th ratio ($D_1/(D_1 + D_2)$) from 0 to 1, where 0 nm represents ZnO/active layer interface (a), the averaged generation rate in the active layer region versus the PTB7-Th ratio (b), maximum theoretical photocurrent J_{ph} and experimental short-circuit current J_{SC} (c) and electrical loss at short-circuit state ($V_{app}=0$) versus PTB7-Th ratio (d).

performance of ternary blend OSCs, quantitatively determine the efficiency change caused by the mentioned mechanisms, and summarize the corresponding design rules based on the theoretical and experimental results for the ternary blend OSCs.

3.1. Carrier generation in ternary blend

Carrier generation process in OSCs includes the photon absorption, exciton generation and dissociation. The photon absorption contributed exciton generation rate is determined by the electromagnetic modeling of the devices including the carrier transport layers and electrodes [32], using the refractive index of each layer measured by the ellipsometer [33], in which the refractive indexes of the ternary blends are shown in Fig. S2. The spatial distributions of generation rate in the active layer with different blend ratios of D_1 component (PTB7-Th) are shown in Fig. 3**(a)**, a significant increase of the generation rate is observed as increasing the ratio of D_1 component. The averaged generation rate in Fig. 3**(b)** reveals that the increase of D_1 component will boost the total generation. The ideal photocurrent can be calculated by the empirical equation $J_{ph}=qGL$, where G is the averaged generation rate, L is the length of the active layer, and q is the elementary charge. Consequently, through conventional empirical model, the photocurrent J_{ph} should obey the trend of the generation rate which augments with an increased ratio of D_1 component. Differently, there is a clear discrepancy between the J_{SC} and the corresponding J_{ph}, while both our theoretical and experimental studies show that the optical loss and electrical loss (particularly caused by delocalization ratio) directly explain the discrepancy which will be detailed as below.

3.1.1. Optical loss

At first, the optical loss occurring during the photon absorption process is calculated by the detailed balance model, which shows the efficiency limit of the solar cells and only depends on the material absorption spectra [1,2]. The framework of the detailed balance model is briefly outlined in the Supplementary Materials. We obtain the limiting short-circuit current J_{limit}, under the assumption of infinite thick active layer. The optical absorption bandgap of the ternary blend is considered as the smaller bandgap of the donor-acceptor combinations. The optical losses of the two binary blend OSCs (D_1/A and D_2/A subsystems) and the ternary blend OSCs are listed in Table 1 and they refer to the current loss at the short-circuit condition, which is defined as $100\%\times(J_{limit}-J_{ph})/J_{limit}$, where $J_{ph}=qGL$. This optical loss indicates the part of incident photon energy which cannot be absorbed by the specific solar cells. It can be seen that the optical loss of ternary blend device (22.59%) is lower than the binary ones, which is 22.76% for D_1/A system and 26.73% for D_2/A system. The introduction of D_1 component in the ternary blend will extend the absorption range, increase the total generation as compared to the binary D_2/A system, and result in the reduction of optical loss. However, the reduced optical loss of

Table 1
Optical loss in binary and ternary blend OSCs.

Device type	D_1/A binary	D_2/A binary	D_1/D_2/A ternary[1]
Optical loss (%)	22.76	26.73	22.59

[1] The ratio of D_1 in the ternary D_1/D_2/A blend is 90% that has the lowest optical loss.

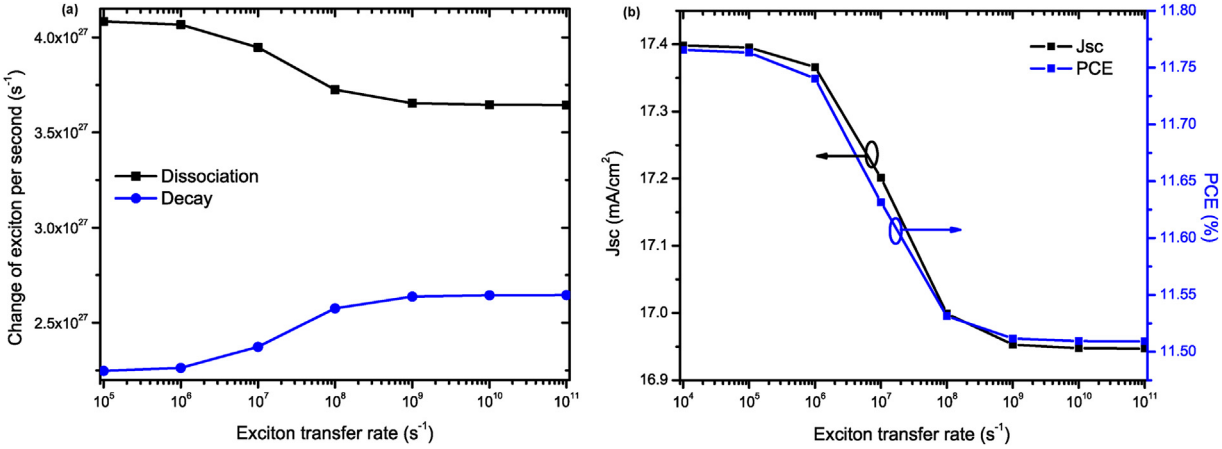

Fig. 4. Theoretical exciton dissociation and decay per second at V_{app} = 0.5 V (a) and short-circuit current J_{SC} and power conversion efficiency (PCE) of the device (b) versus the exciton transfer rate. The ratio of the D_1 and D_2 in the simulation is set as D_1:D_2 = 1:1.

ternary D_1/D_2/A blend (~ 4.14%) cannot contribute to such significant improvement of experimental J_{SC} (~ 30%, see inset of Fig. 2) of ternary blend OSCs. Consequently, our result indicates that not only the optical properties, but also the electrical properties of exciton and charge carriers play an important role in the efficiency improvement.

3.1.2. Electrical loss

As we know, the difference between the photo-generated current J_{ph} and short circuit current J_{SC} are mainly due to inefficient dissociation of the excitons. Theoretically, the electrical loss caused by the inefficient dissociation of excitons can be indicated by the discrepancy between the J_{SC} and the corresponding J_{ph}, which is defined as 100%×(J_{ph}-J_{SC})/J_{ph}. The experimental J_{SC} and the maximum theoretical photocurrent J_{ph} for ternary blend OSCs of different PTB7-Th ratios are shown in Fig. 3**(c)** and the electrical loss is shown in Fig. 3**(d)**. Generally, the dissociation probability of the localized exciton at D_1/A and D_2/A interfaces stay constant, the electrical loss should be linearly changed with the component ratio in the case that the exciton delocalization mechanism is not considered. Interestingly, a turning point at 70% ratio and the changing slope of the curve are observed in Fig. 3(d) (resulting into the best performed ternary OSCs at 70% ratio as shown in Fig. 2 and the inset Table), which suggests that the change of electrical loss is critically correlated to the effect of exciton delocalization.

The delocalization ratio change of the ternary active layer under different component ratios is very important but limited studied. As observed in binary organic blend, the promotion of exciton delocalization would directly favor the carrier generation resulting in linearly increasing J_{SC} and PCE. The higher delocalization ratio of the total generated excitons, the lower energy loss caused by the localized exciton decay [17]. In this work, we have introduced the effect of delocalization in the ternary blend OSCs to interpret the reduction point shown in Fig. 3(d). Through combining the theoretical modeling results with the experimental results, we will unveil that the lower electrical loss at 70% PTB7-Th ratio is mainly attributed to the higher delocalization ratio, which highlight the importance of improving the delocalization ratio in ternary blend. Since delocalization effect can be represented by the experimental J-V characteristics, we will elucidate the detailed delocalization effect in Section 3.4.

3.2. Exciton (energy) transfer in ternary blend

The optimization of the ternary blend OSCs lies at the reduction of the energy loss caused by several processes, including exciton decay and bulk recombination. When the D_1 ratio increases from 0% to 100%, the localized exciton dissociation may occur in two donor/acceptor interfaces with different dissociation rates and probabilities. In the meantime, both of the exciton and hole transfer processes may occur in the mixed ternary blend which is very different from binary blend systems, exciton transfer process will be studied in this section and the hole transfer process will be discussed in the next section.

The exciton transfer direction between two donors can be determined by the overlap of their PL and absorption spectra. As confirmed by the PL and absorption spectra of the two polymers and the PL of their blend (See Fig. 1), the PL spectrum of D_2 (peak at 720 nm) has a good overlap with the absorption spectrum of D_1 (peak at 710 nm), while the PL spectrum of D_1 (peak at 840 nm) is far away from the absorption spectrum of D_2 (peak at 590 nm). Based on the Förster energy transfer theory, the good overlapping of the PL spectrum of D_2 and the absorption spectrum of D_1 will lead to a large Förster energy transfer radius, therefore a large energy transfer rate. In addition, the PL spectrum of the D_1:D_2 blend is similar to that of D_1 PL, which also indicates excitons move from D_2 to D_1 before they radiatively recombine. Consequently, our results show that the non-radiative exciton transfer exists in the blend, but only the transfer from D_2 to D_1 is allowed, which will result in extra carrier loss and reduce the J_{SC}. To further study the effect of the exciton transfer, we have simulated ternary blend OSCs and their results are discussed below.

As shown in Fig. 3(d), the electrical loss of binary D_1/A subsystem is larger than that of D_2/A counterpart, which indicates the localized exciton dissociation at the D_1/A interface is less efficient than that at D_2/A interface. However, the exciton transfer process enables the exciton generated in D_2 to diffuse towards D_1, and then to dissociate or decay at D_1/A interface. The effect of this process is shown in Fig. 4. With the increase of exciton transfer rate in the ternary blend, the number of dissociated excitons will reduce, but conversely increase the number of the decayed excitons, implying the total energy loss in the solar cells become significant. Therefore, the J_{SC} decreases from 17.39 mA cm^{-2} to 16.95 mA cm^{-2} by 3%. Since exciton energy loss has ignorable effects on the carrier extraction process and the bulk recombination, the V_{OC} only reduces 3 mV, and the fill factor only decrease by 1% (not shown). As a result, the decrease of PCE from 11.77% to 11.51% by 0.26% is mainly due to the reduction of J_{SC}. When the exciton transfer rate increases to the order of 10^9 s^{-1}, the change of device performance parameters will saturate, because the most part of the excitons in D_2 have already transferred to D_1. Consequently, the exciton transfer in our device will reduce the total amount of generated carrier, resulting in a lower J_{SC} and PCE. However, if the PL spectrum of D_1 can overlap well with the absorption spectrum of D_2 and the exciton transfer direction is from D_1 to D_2, we can expect a higher J_{SC} from the beneficial exciton transfer. Therefore, selecting the materials with proper overlapping of the PL and absorption spectra as mentioned will improve the J_{SC} and thus PCE.

3.3. Hole transfer between donors in ternary blend

Apart from the mechanisms during the carrier generation process, the ternary blend structure will also influence the carrier transport. The hole transfer between D_1 and D_2 will affect device performances in terms of different recombination rate coefficient (γ) and carrier mobility [27]. The hole transfer from acceptor to donor which may exist in some D/A systems is not considered here since it is not related to the unique properties based on the ternary blend structure, i.e. differences between two donors. The lower recombination rate coefficient and higher mobility in D_2/A subsystem channel make it facilitate the carrier transport, while the carrier transport in D_1/A subsystem channel will suffer from a larger recombination loss. In order to confirm the existence of the hole transfer between the donors, the hole-only devices based on single-layer and double-layer of D_1 and D_2 have been fabricated and measured. The J-V characteristics of the hole-only devices are measured under the forward and backward bias voltages, and the symmetric J-V curves are observed for both the devices with single-layer and double-layer of D_1 and D_2, as shown in Fig. S3. These results indicate that the hole transfers from D_1 to D_2 and from D_2 to D_1 are all available, although the HOMO offset (0.06 eV) exists between the two donors. Therefore, in our analysis, the transfers of the holes from D_1 to D_2 and from D_2 to D_1 exist simultaneously and the cancellation of each other will result in a net hole transfer. The influences of the net hole transfer both from D_1 to D_2 and D_2 to D_1 are shown in Fig. 5.

It should be noted that the recombination rate R is the product of recombination rate coefficient γ and the carrier density ($n \times p$), as shown in Eq. (A6). The results show that the hole transfer from the "better" channel to the "worse" channel will induce the extra loss. When holes transfer from D_2 to D_1, the transfer of the carriers to the worse D_1/A subsystem channel will substantially increase the bimolecular (bulk) recombination. Meanwhile, the reduction of the hole density in the other better channel cannot contribute to reduce the total recombination due to its already small recombination rate coefficient γ. Therefore, as shown in Fig. 5(a), in this worse case of hole transfer (D_2 to D_1), the total recombination in the device will increase that will decrease the device performance. On the contrary, in the better case of hole transfer (D_1 to D_2), the transfer from the worse subsystem channel to the better one will reduce the overall recombination, and increase the performance. The increment of V_{OC} and fill factor from the worse case to the better case can be up to 20 mV and 4%, respectively. Consequently, controlling the hole transfer direction is critical, i.e. by engineering the energy level alignment to enhance the beneficial hole transfer rate and form a blocking barrier for eliminating the disadvantageous hole transfer into worse subsystem channel with high recombination loss.

3.4. Theoretical and experimental understanding of overall performances

After understanding the physics and effects of the carrier generation, exciton and hole transfer from Sections 3.1 to 3.2, we can theoretically and experimentally evaluate the overall device performances. The carrier generation and transport mechanisms of the ternary blend OSCs under different component ratio can be obtained and analyzed with the proposed device modeling. The delocalization ratio (η_d, in Eqs. (A2)–(A4), (A8) and (A9)), exciton transfer rates ($\upsilon_{1,2}$, in Eqs. (A8) and (A9)) and hole transfer rates ($\sigma_{1,2}$, in Eqs. (A3) and (A4)) can be determined by carefully fitting the results from modeling and experiment. As discussed previously, the exciton transfer has a significant influence on the free carrier generation and thus J_{SC}, while the hole transfer shows more impact on the carrier transport and thus V_{OC} and fill factor. The delocalization ratio will simultaneously and near linearly change the J_{SC}, V_{OC}, fill factor, and PCE. The theoretical results are well-agreed with the experimental results as shown in Fig. 6 for understanding the physics of carrier generation and transport as described below.

The experimental J_{SC}, V_{OC}, fill factor and PCE in Fig. 6 are summarized from Fig. 2. From the theoretical results, the device physics can be clearly unveiled by the ratio of delocalization exciton (η_d), the exciton transfer rate (υ_2) and the hole transfer rate (σ_1) determined as in Fig. S4. By introducing the D_1 (PTB7-Th) component into the active blend, the delocalization ratio decreases at the beginning, but when D_1 ratio further increases, the delocalization ratio increases and peaks at the optimized D_1 ratio 70%. The high delocalization ratio at 70% D_1 ratio should be attributed to the good morphology, which can be supported by the highest and balanced electron and hole mobilities at this ratio (See in Table S1). Since there is no overlap between D_1 PL and D_2 absorption spectrum, the exciton transfer from D_1 to D_2 is forbidden (i.e. $\upsilon_1 = 0$). Meanwhile, the allowed exciton transfer from D_2 to D_1 first increases and then decreases and the peak point reaches at the D_1 ratio of 70%. Although the two-way hole transfers are all possible, through the theoretical and experimental studies, we confirm that the effective hole transfer direction is from D_1 to D_2, and the hole transfer rate also reaches the maximum at the ratio of 70%.

With the above theoretical and experimental results, the PCE of the ternary blend OSCs reveals a clear correlation with three parameters of delocalization exciton ratio, the exciton transfer rate and the hole transfer rate, which corresponds to the three physical processes of the ultrafast and efficient free carrier generation from delocalized exciton, the unexpected exciton transfer from D_2 to D_1 and the advantageous hole transfer from D_1 to D_2, respectively. The PCE change (ΔPCE) of the ternary blend OSC has been quantitatively evaluated in Table 2, in which $\Delta PCE = 100\% \times (\eta - \eta^*)/\eta$, η is the theoretical PCE taking into account all the three physical processes, which matching the

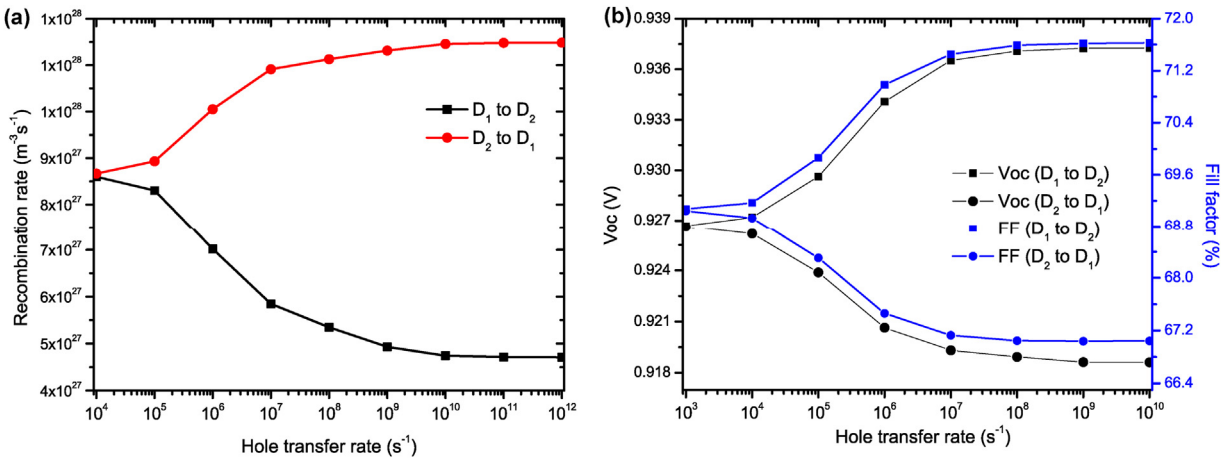

Fig. 5. The change of recombination rate R at $V_{app} = 0.5$ V (a) and the V_{OC} and fill factor (b) versus the hole transfer rate. The ratio of the D_1 and D_2 in the simulation is set as D_1:D_2 = 1:1.

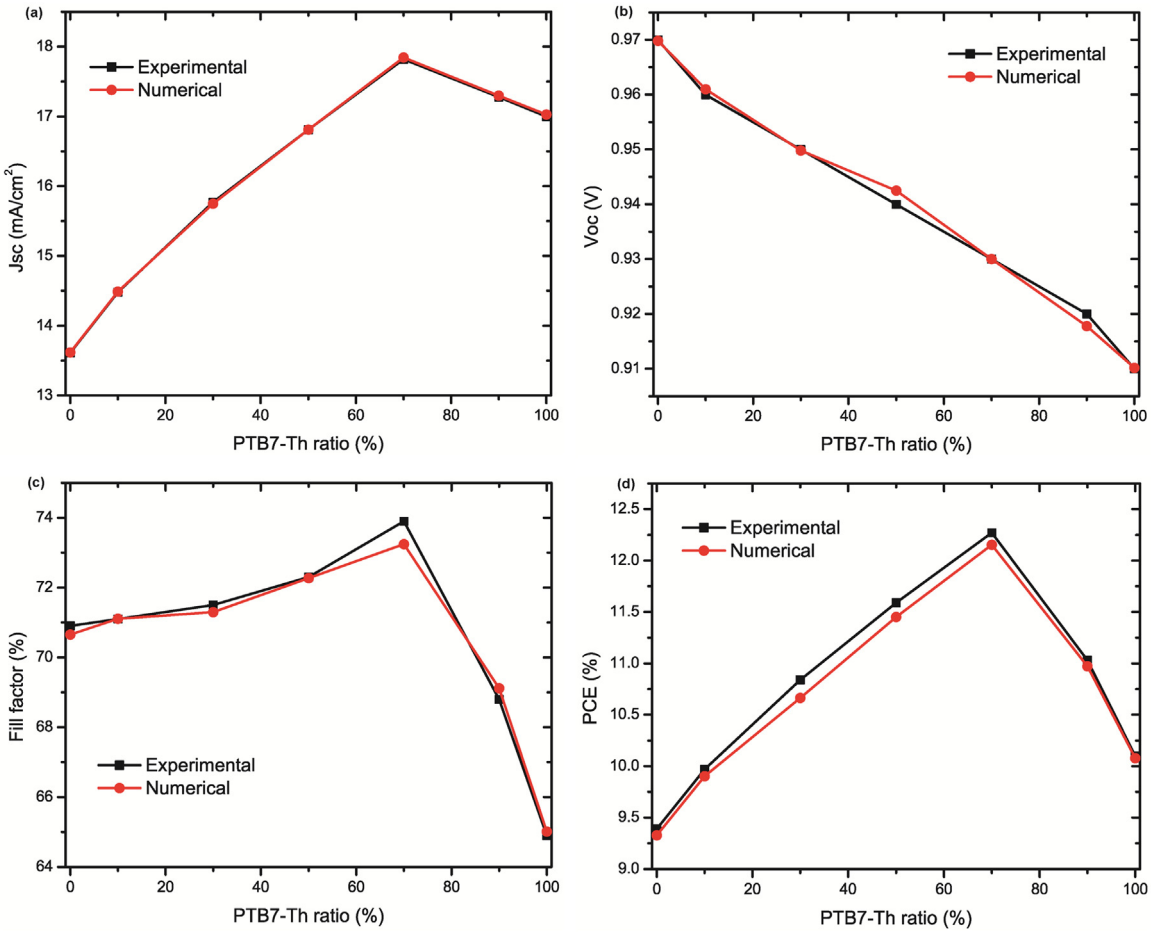

Fig. 6. Comparison of the numerical and the experimental results with different PTB7-Th ratios: J_{SC} (a), V_{OC} (b), fill factor (c), PCE (d).

Table 2
The PCE change (ΔPCE) in ternary blend OSCs with different D_1 ratios (i.e. $D_1/(D_1 + D_2)$) caused by A: inefficient free carrier generation, B: undesirable exciton transfer from D_2 to D_1 and C: the advantageous hole transfer from D_1 to D_2.

D_1 ratio	10%	30%	50%	70%	90%
ΔPCE by A	− 21.94%	− 23.62%	− 22.42%	**− 20.85%**	− 27.44%
ΔPCE by B	− 3.41%	− 2.23%	− 1.90%	**− 1.12%**	− 0.47%
ΔPCE by C	+ 0.51%	+ 2.71%	+ 3.30%	**+ 5.43%**	+ 2.16%

experiments, and η^* is the theoretical PCE without the specific physical process. Negative sign of ΔPCE means that there is a PCE loss while positive sign of ΔPCE indicates there is PCE enhancement. It should be noted that the case (A) show ΔPCE excluding the effect of localized exciton i.e. delocalization ratio = 100%, implying that ΔPCE is due to the inefficient free carrier generation caused by the localized exciton. Our results show that, in case (A), the loss caused by inefficient free carrier generation is minimum at D_1 ratio of 70%. The best performance mainly benefits from the efficient free carrier generation, i.e. ultrafast carrier generation by delocalized exciton. In case (B), the loss from the exciton transfer from D_2 to D_1 decreases continuously when D_1 ratio increases. It is because the increased total amount of excitons from the boosted exciton generation rate will enlarge the amount of free carrier, and thus compensate the detrimental influence of exciton transfer. In case (C), the enhancement from the hole transfer reaches the maximum at D_1 ratio of 70% condition, since the largest hole transfer rate from D_1 to D_2 at this condition reduces most the recombination loss.

According to our theoretical results, the main improvement of the ternary blend OSCs is from the more efficient carrier generation by localized exciton dissociation and delocalization process. Meanwhile, from the above experimental and theoretical studies, we summarize the general design rules to improve device efficiency of ternary blend OSCs. (1) As discussed in Section 3.1, a better exciton delocalization via donor ratio optimization is beneficial to more efficient carrier generation, which is the most important way to improve J_{SC} and thereby the device performance of ternary blend OSCs. (2) Since the overlap between the emission and absorption spectra of the donor materials determine the exciton transfer direction, the selection of donor materials needs to ensure good overlap of the absorption spectrum of the donor material with the high exciton dissociation probability at the D/A interfaces and the PL spectrum of another donor material, which will increase J_{SC}. (3) Since hole transfer inside the ternary blend OSCs to the donor with large recombination rate will cause extra loss, the engineering of the energy level alignment of donors needs to be applied to form the blocking barrier. This can inhibit the disadvantageous hole transfer to the donor with large recombination rate and will reduce the recombination loss resulting in the increase of the V_{OC} and fill factor.

With the three design rules, the ternary blend OSCs can benefit from the wide absorption range, large exciton generation rate, lower recombination rate, high exciton dissociation efficiency, and thus reach a high PCE. These advantages are based on the unique structure of ternary blend OSCs, and cannot be reached by the solar cells with similar principles like tandem solar cells, due to the lack of the exciton and carrier transfer between the components, and the existence of the challenges in the interfaces contact.

4. Conclusion

We have conducted the comprehensively theoretical and experimental studies of carrier generation and transport in ternary blend OSCs. We have clarified the carrier generation (exciton transfer, delocalization and dissociation) and transport processes in the ternary blend OSCs. Meanwhile, the high-performance non-fullerene acceptor ternary blend OSCs made from of PTB7-Th (D_1)/PBDB-T (D_2)/SFBRCN (A) system have been fabricated for understanding the device physics. Our results indicate the improvement of the performance of ternary blend OSCs is not only attributed to the reduction of optical loss, but also to the optimization of the exciton and carrier behavior. The carrier generation and transport have been analyzed in details. Our results show that the transfer directions of the exciton and hole transfer in donors will have a significant influence on device performances due to the unbalanced exciton dissociation probability and recombination strength in the different donor: acceptor combinations. We have also summarized three guidelines for ternary blend OSCs. (1) The larger delocalization ratio favors the carrier generation and results in a higher J_{SC}, which is well supported by the experimentally fitted parameters of delocalization ratio. Improving the delocalization ratio via donor ratio optimization with physical understanding is highly important for promoting efficient carrier generation. (2) The well overlap between D_2 PL spectrum and D_1 absorption spectrum introduces the localized exciton transfer from D_2 to D_1, which causes an extra loss of J_{SC} because of the insufficient exciton dissociation probability at D_1/A interface suggested by the experimental results. This finding can be applied to other D_1/D_2/A (A_1/A_2/D) ternary blend systems by carefully selecting the donors (acceptors) materials with appropriate overlap between the PL and absorption spectra to control the exciton transfer direction, and reduce the loss. (3) Since D_2 has a small recombination rate and high carrier mobility that favors the carrier extraction, the theoretical and experimental results show that the net hole transfer from D_1 to D_2 will reduce the total recombination loss and thus increase the V_{OC} and fill factor. In other D_1/D_2/A (A_1/A_2/D) ternary blend systems, the engineer of energy level alignment of the donors (acceptors) material to form the blocking barrier can control the net carrier transfer direction, and increase the performance. Our work contributes to unveil the insight of device physics and propose the new design rules for achieving high-performance ternary OSCs.

Acknowledgements

This work was supported by the University Grant Council of the University of Hong Kong (Grants 201611159194 and 201511159225), the General Research Fund (Grants 711813 and 17211916), the Collaborative Research Fund (Grant C7045-14E) from the Research Grants Council of Hong Kong Special Administrative Region, China, ECF Project 33/2015 from Environment and Conservation Fund, and Grant CAS14601 from CAS-Croucher Funding Scheme for Joint Laboratories.

Appendix A. Theoretical modeling details

The semiconductor carrier transport model based on the drift-diffusion equations has been widely used in the multi-physical simulation of solar cells [34,35]. In our model, the governing equations are shown as follows:

$$\nabla\cdot(\varepsilon\nabla\varphi) = -q(p_1 + p_2 - n) \tag{A1}$$

$$\frac{\partial n}{\partial t} = \eta_d G + \frac{1}{q}\nabla\cdot\left(q\mu_n n E_n + qD_n\nabla n\right) + k_1X_1 + k_2X_2 - R_1 - R_2 \tag{A2}$$

$$\frac{\partial p_1}{\partial t} = \alpha\eta_d G - \frac{1}{q}\nabla\cdot\left(q\mu_{p1}p_1E_p + qD_{p1}\nabla p_1\right) + k_1X_1 - R_1 + \sigma_2p_2 - \sigma_1p_1 \tag{A3}$$

$$\frac{\partial p_2}{\partial t} = \left(1-\alpha\right)\eta_d G - \frac{1}{q}\nabla\cdot\left(q\mu_{p2}p_2E_p + qD_{p2}\nabla p_2\right) + k_2X_2 - R_2 + \sigma_1p_1 - \sigma_2p_2 \tag{A4}$$

where p_1, p_2, and n are the densities of hole in D_1, D_2 and A respectively, q is the electronic charge, μ_n, and μ_p are the electron and hole mobility respectively, and D_n, and D_p are the electron and hole diffusion coefficients, respectively, which obey the Einstein relation:

$$D_{n,p} = \frac{k_BT}{q}\mu_{n,p} \tag{A5}$$

where k_B is the Boltzmann constant, and T is the absolute temperature. E_n, and E_p are the internal electrostatic fields for electron and hole, considering the effect of the injection and extraction barriers at the interfaces. η_d is the delocalization ratio, and G is the exciton generation rate in the active layer. The separation of the delocalized exciton is highly efficient and rapid, thus it will be considered as the direct generation of the free carriers [17].

The component ratio $D_1/(D_1 + D_2)$ in our model is denoted by the factor α, which modulates the generation rate in Eqs. (A3) and (A4). Each component in the active layer will absorb photons individually, and thus it will be a proper approximation to modulate the generation rate by the component ratio under an assumption that the components in the blends are mixed uniformly. The introduction of this factor also indicates that the ratio $D_1/(D_1 + D_2)$ will directly influence the vertical distribution of the donors and acceptor, so that the carrier transport and collection. σ_1, σ_2 are the hole transfer rates from D_1 to D_2 and D_2 to D_1, respectively, and the loss occurring during the transfer is ignored. $R_{1(2)}$ represent the bimolecular recombination between n and $p_{1(2)}$ respectively, which obey the form:

$$R = r_R\cdot\gamma(np - n_i^2) \tag{A6}$$

where n_i is the intrinsic carrier density of the active material. γ is recombination coefficient by Langevin [36]:

$$\gamma = q\frac{\langle\mu\rangle}{\langle\varepsilon\rangle} \tag{A7}$$

where $<\mu>$ is the spatial averaged summation of hole and electron mobility, and $<\varepsilon>$ is the spatial averaged dielectric constant. The factor r_R is a coordination factor introduced to reduce the recombination rate given by Langevin theory [36], which is much larger than that in experiment

Table A1
The list of the parameters used in the simulation.

Parameters	Symbol	Numerical Value
Exciton lifetime in D_1/A	τ_1	92.7 ps [27]
Exciton lifetime in D_2/A	τ_2	165.9 ps [27]
Exciton radius	a	1.7 nm
Exciton diffusion length	L	8.5 nm [40]
Average dielectric constant	ε	3.9
Carrier mobility	$\mu_{n,p}$	See in Table S1
Temperature	T	300 K
Generation rate	G	See in Fig. 3
Effective density of state	$N_c(N_v)$	2.5×10^{25} m^{-3}
Bandgap of D_1/A	Eg_1	1.41 eV [27]
Bandgap of D_2/A	Eg_2	1.47 eV [27]

[37,38]. Here r_R is set as 1×10^{-3} in the simulation.

The parameters k_1 and k_2 are the localized singlet exciton dissociation rate, given by the Onsager-Braun model, and X_1 and X_2 are the concentrations of the singlet excitons which will dissociate at the D_1/A or D_2/A interfaces. The behavior of the excitons is described by the augmented diffusion-reaction equations:

$$\frac{\partial X_1}{\partial t} = \alpha\left(1-\eta_d\right)G + \nabla\cdot\left(D_{x1}\nabla X_1\right) - k_1X_1 - \frac{X_1}{\tau_1} + \eta_s R_1 + \upsilon_2 X_2 - \upsilon_1 X_1 \tag{A8}$$

$$\frac{\partial X_2}{\partial t} = \left(1-\alpha\right)\left(1-\eta_d\right)G + \nabla\cdot\left(D_{x2}\nabla X_2\right) - k_2X_2 - \frac{X_2}{\tau_2} + \eta_s R_2 + \upsilon_1 X_1 - \upsilon_2 X_2 \tag{A9}$$

where $D_{x1\ (x2)}$ are the exciton diffusion coefficients obtained from the equation $L = \sqrt{D_{x1(x2)}\tau_{1(2)}}$. The empirical exciton diffusion length L is considered as *8.5 nm*, as shown in ref. 28. The $(1\text{-}\eta_d)$ part of the exciton generation rate will form the localized excitons, and they may diffuse to the donor/acceptor interface through the Förster energy transfer. At the interface, they will dissociate at the rates $k_{1,2}$, or decay to the ground state in the lifetime $\tau_{1,2}$. The bimolecular recombination of the free carriers will regenerate the localized exciton, and only the singlet exciton will be considered in the model, with the amount ratio of $\eta_s = 1/4$. The exciton transfer from D_1 to D_2 and from D_2 to D_1 are represented by the rate factor $\upsilon_{1,\ 2}$.

The charge collection properties are modeled by setting the multi-layered device structure including the carrier transport layers and the electrodes. We considered the charge injection/extraction effects by including the injection/extraction barriers in the internal electrostatic fields E_n *and* E_p. We set $x = 0$ as the top cathode of the device, where x denotes the position, and set $x = L$ as the bottom anode, where L is the device thickness. The boundary conditions for the Poisson equation is determined by the work functions of the cathode and anode, as well as the Schottky barrier between the electrodes and the charge transporting layers, as shown below:

$$\varphi(0) = -W_C - U_{BN},\ \varphi(L) = V_a - W_A + U_{BP} \tag{A10}$$

where $W_{C,(A)}$ is the work functions of cathode (anode), $U_{BP,(BN)}$ is the Schottky barrier at the interfaces between carrier transporting layers and cathode (anode), and V_a is the applied voltage. The boundary conditions of electron and hole densities are:

$$n(0) = N_C\exp\left(-\frac{U_{BN}}{k_BT}\right),\ n(L) = N_C\exp\left[\frac{(U_{BP}-E_g)}{k_BT}\right] \tag{A11}$$

$$p_{1,2}(0) = N_V\exp\left[\frac{(U_{BN}-E_g)}{k_BT}\right],\ p_{1,2}(L) = N_V\exp\left(-\frac{U_{BP}}{k_BT}\right) \tag{A12}$$

where $N_{C,(V)}$ is the effective density of states of conduction (valence) band of the carrier transporting layers, and E_g is the bandgap.

The excitons will quench at the interfaces between the active layer and carrier transport layers ($x = d_1$, $x = d_2$):

$$X_{1,2}(d_1) = X_{1,2}(d_2) = 0 \tag{A13}$$

Eqs. (A1)–(A4) and (A8) and (A9) will be solved by the finite-difference method using the semi-implicit strategy in time domain [32]. For spatial domain, Scharfetter-Gummel scheme is used [39]. The detailed discretization form will be shown in supplementary material. The parameters used in this model are shown in Table A1. The energy level schematic and the device structure are shown in Fig. S5.

Appendix B. Supplementary material

Supplementary data associated with this article can be found in the online version at http://dx.doi.org/10.1016/j.nanoen.2018.06.069.

References

[1] W. Shockley, H.J. Queisser, J. Appl. Phys. 32 (1961) 510–519.
[2] W.E.I. Sha, X. Ren, L. Chen, W.C.H. Choy, Appl. Phys. Lett. 106 (2015) 221104.
[3] H. Benten, T. Nishida, D. Mori, H. Xu, H. Ohkita, S. Ito, Energy Environ. Sci. 9 (2016) 135–140.
[4] T. Kumari, S.M. Lee, S.-H. Kang, S. Chen, C. Yang, Energy Environ. Sci. 10 (2017) 258–265.
[5] P. Cheng, C. Yan, T.-K. Lau, J. Mai, X. Lu, X. Zhan, Adv. Mater. 28 (2016) 5822–5829.
[6] P. Cheng, R. Wang, J. Zhu, W. Huang, S.-Y. Chang, L. Meng, P. Sun, H.-W. Cheng, M. Qin, C. Zhu, X. Zhan, Y. Yang, Adv. Mater. 1705243-n/a.
[7] P. Cheng, C. Yan, Y. Wu, J. Wang, M. Qin, Q. An, J. Cao, L. Huo, F. Zhang, L. Ding, Y. Sun, W. Ma, X. Zhan, Adv. Mater. 28 (2016) 8021–8028.
[8] P. Cheng, M. Zhang, T.-K. Lau, Y. Wu, B. Jia, J. Wang, C. Yan, M. Qin, X. Lu, X. Zhan, Adv. Mater. 29 (2017) (1605216-n/a).
[9] Y. Yang, W. Chen, L. Dou, W.-H. Chang, H.-S. Duan, B. Bob, G. Li, Y. Yang, Nat.

Photonics 9 (2015) 190–198.
[10] Q. An, F. Zhang, J. Zhang, W. Tang, Z. Deng, B. Hu, Energy Environ. Sci. 9 (2016) 281–322.
[11] S.A. Mollinger, K. Vandewal, A. Salleo, Adv. Energy Mater. 5 (2015) (1501335-n/a).
[12] Z. Xiao, X. Jia, L. Ding, Sci. Bull. 62 (2017) 1562–1564.
[13] H. Li, Z. Xiao, L. Ding, J. Wang, Sci. Bull. 63 (2018) 340–342.
[14] P.P. Khlyabich, B. Burkhart, B.C. Thompson, J. Am. Chem. Soc. 133 (2011) 14534–14537.
[15] R.A. Street, D. Davies, P.P. Khlyabich, B. Burkhart, B.C. Thompson, J. Am. Chem. Soc. 135 (2013) 986–989.
[16] B.M. Savoie, S. Dunaisky, T.J. Marks, M.A. Ratner, Adv. Energy Mater. 5 (2015) (1400891-n/a).
[17] Z.S. Wang, W.E.I. Sha, W.C.H. Choy, J. Appl. Phys. 120 (2016) 213101.
[18] L.G. Kaake, D. Moses, A.J. Heeger, Phys. Rev. B 91 (2015) 075436.
[19] S. Gélinas, A. Rao, A. Kumar, S.L. Smith, A.W. Chin, J. Clark, T.S. van der Poll, G.C. Bazan, R.H. Friend, Science 343 (2014) 512–516.
[20] A.C. Jakowetz, M.L. Böhm, J. Zhang, A. Sadhanala, S. Huettner, A.A. Bakulin, A. Rao, R.H. Friend, J. Am. Chem. Soc. 138 (2016) 11672–11679.
[21] A.E. Jailaubekov, A.P. Willard, J.R. Tritsch, W.-L. Chan, N. Sai, R. Gearba, L.G. Kaake, K.J. Williams, K. Leung, P.J. Rossky, X.Y. Zhu, Nat. Mater. 12 (2013) 66–73.
[22] D.M. Stoltzfus, J.E. Donaghey, A. Armin, P.E. Shaw, P.L. Burn, P. Meredith, Chem. Rev. 116 (2016) 12920–12955.
[23] G. Zhang, G. Yang, H. Yan, J.-H. Kim, H. Ade, W. Wu, X. Xu, Y. Duan, Q. Peng, Adv. Mater. 29 (2017) (1606054-n/a).
[24] D.P. Qian, L. Ye, M.J. Zhang, Y.R. Liang, L.J. Li, Y. Huang, X. Guo, S.Q. Zhang, Z.A. Tan, J.H. Hou, Macromolecules 45 (2012) 9611–9617.
[25] C.L. Braun, J. Chem. Phys. 80 (1984) 4157–4161.
[26] L. Onsager, J. Chem. Phys. 2 (1934) 599–615.
[27] X. Xu, Z. Bi, W. Ma, Z. Wang, W.C.H. Choy, W. Wu, G. Zhang, Y. Li, Q. Peng, Adv. Mater. 29 (2017) (1704271-n/a).
[28] T. Kirchartz, J. Nelson, U. Rau, Phys. Rev. Appl. 5 (2016) 054003.
[29] S. Gao, L. Bu, Z. Zheng, X. Wang, W. Wang, L. Zhou, J. Hou, G. Lu, AIP Adv. 7 (2017) 045312.
[30] B. Godefroid, G. Kozyreff, Phys. Rev. Appl. 8 (2017) 034024.
[31] J.C. Blakesley, D. Neher, Phys. Rev. B 84 (2011) 075210.
[32] W.E.I. Sha, W.C.H. Choy, Y. Wu, W.C. Chew, Opt. Express 20 (2012) 2572–2580.
[33] C.H.C. Wallace, H.H. Fong, J. Phys. D: Appl. Phys. 41 (2008) 155109.
[34] A. Shang, X. Li, Adv. Mater. 29 (2017) (1603492-n/a).
[35] X. Li, N.P. Hylton, V. Giannini, K.-H. Lee, N.J. Ekins-Daukes, S.A. Maier, Progress. Photovolt.: Res. Appl. 21 (2013) 109–120.
[36] P. Langevin, Ann. Chim. Phys. 28 (1903) 122.
[37] M. Hilczer, M. Tachiya, J. Phys. Chem. C 114 (2010) 6808–6813.
[38] T.M. Burke, S. Sweetnam, K. Vandewal, M.D. McGehee, Adv. Energy Mater. 5 (2015) (1500123-n/a).
[39] D.L. Scharfetter, H.K. Gummel, IEEE, Trans. Electron Dev. 16 (1969) 64–77.
[40] P.E. Shaw, A. Ruseckas, I.D.W. Samuel, Adv. Mater. 20 (2008) 3516–3520.

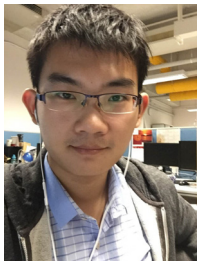

Zishuai Wang received his bachelor degree in the School of Optical Information from the University of Electronic Science and Technology of China in 2015. Currently, he is studying Ph.D.program in department of Electrical and Electronic Engineering in the University of Hong Kong. His current research interests include the device modeling of the emerging photovoltaic devices.

Xingang Ren received the B.S. in Mathematics and Applied Mathematics and M.S. in Electromagnetic Field and Microwave Technology from Anhui University, Hefei, China in 2009 and 2012, respectively. He received his Ph.D. degree from the Department of Electrical and Electronic Engineering (EEE), the University of Hong Kong (HKU). His research interests include the nano-optics and physics of organic optoelectronics.

Xiaopeng Xu received his B.S. degree in the College of Resources and Environmental Engineering from Heilongjiang University of Science and Technology in 2013 and his M.S. degree in the College of Chemistry from Sichuan University in 2016. Currently, he is a Ph.D. candidate under the supervision of Prof. Qiang Peng in Sichuan University. His research interests include the organic optoelectronic materials design and photovoltaic devices engineering.

Qiang Peng received his Ph.D. degree from Sichuan University, China, in 2004. He joined National University of Singapore (NUS) as a postdoctoral researcher from 2004 to 2006. After that, he moved to University of Dayton as a postdoctoral researcher in November 2006. In 2008, he joined Nanchang Hangkong University as full professor in the School of Environment and Chemical Engineering. Since 2011, he has been a full professor in the College of Chemistry, Sichuan University, China. His research interests include organic optoelectronic materials and devices, such as organic light emitting diodes and organic solar cells.

Wei E.I. Sha received the B.S. and Ph.D. degrees in Electronic Engineering at Anhui University, Hefei, China, in 2003 and 2008, respectively. From Jul. 2008 to Jul. 2017, he was a Postdoctoral Research Fellow and then a Research Assistant Professor in the Department of Electrical and Electronic Engineering at the University of Hong Kong, Hong Kong. Now, he is an Assistant Professor in the College of Information Science & Electronic Engineering at Zhejiang University, Hangzhou, China. He engages in theoretical and computational research in electromagnetics and optics, focusing on the multiphysics and interdisciplinary areas. His research involves fundamental and applied aspects in plasmonics, emerging photovoltaics, metasurfaces, quantum electrodynamics, and computational electromagnetics.

Wallace C.H. Choy received his Ph.D. Degree in Electronic Engineering from University of Surrey, UK in 1999. He is now a Professor in Department of EEE, HKU. His research interests cover organic/inorganic optoelectronic devices, plasmonic structures, metal oxides, and nanomaterial devices. He has published more than 170 peer-reviewed papers, a number of book chapters, patents, and edited one book published in Springer. He was recognized as the Top 1% of most-cited scientists in Thomson Reuter's Essential Science Indicators from 2014 to 2016. He is serving as editorial board member of NPG Scientific Reports and IOP J Physics D, topical editor of OSA JOSA B, and senior editor of IEEE Photonic Journals. He is an elected fellow of OSA.